Journal of Power Sources 196 (2011) 4686–4694

Contents lists available at ScienceDirect

Journal of Power Sources

journal homepage: www.elsevier.com/locate/jpowsour

Interfacial failure via encapsulation of external particulates in an outward-growing thermal oxide

Keeyoung Jung[a,b,*], Chang-Soo Kim[c], Frederick S. Pettit[a,b], Gerald H. Meier[a,b]

[a] National Energy Technology Laboratory, Pittsburgh, PA 15236, United States
[b] Department of Mechanical Engineering and Materials Science, University of Pittsburgh, Pittsburgh, PA 15261, United States
[c] Materials Department, University of Wisconsin-Milwaukee, Milwaukee, WI 53211, United States

ARTICLE INFO

Article history:
Received 23 November 2010
Received in revised form
20 December 2010
Accepted 21 December 2010
Available online 12 January 2011

Keywords:
Syngas
Oxidation
Chromia former
Buckling
Numerical analysis
Finite element analysis

ABSTRACT

A Cr_2O_3-forming Ni-base superalloy and this alloy coated with a Pt-modified aluminide coating were exposed to SiO_2 powder and cyclically oxidized at 950 °C. The uncoated alloy showed a considerable amount of spallation and buckling whereas the Pt–NiAl coated alloy remained protective throughout hundred 1 h-cycles. The interfacial failure is mainly ascribed to the increased thermal strain by the encapsulation of external SiO_2 particulates in an outward-growing Cr_2O_3 layer. However, the particles were not embedded in the thermally grown oxide of the Pt–NiAl coated alloy due to the slow inward-growing characteristics of Al_2O_3 scales. The buckling of the Cr_2O_3 scale with embedded SiO_2 was analyzed with (1) a classical buckling criterion using the instantaneous coefficients of thermal expansion of the constituents, and (2) finite element analyses (FEA) to estimate the local interfacial shear stresses. It turns out that the thermal strain with embedded SiO_2 is larger than the experimentally determined critical thermal strain (ε_b) explaining the buckling of the oxide scale observed in the experiment. The FEA results demonstrate that local shear stresses at the metal/oxide interface are significantly amplified near the SiO_2 particles showing that the buckling of oxide can be readily initiated especially in the vicinity of the embedded particles.

1. Introduction

When syngas derived from coal or other practicable sources are used in gas turbines or solid oxide fuel cells (SOFCs), inorganic ash can form and accumulate on interior hardware which may cause accelerated corrosion [1,2]. The composition of the ash from coal or coal-derived gas combustion mostly contains oxide compounds such as SiO_2, Al_2O_3, Fe_2O_3, and CaO. The amounts of these deposit particulates are expected to be reduced by clean-up processes, but vary depending on the effectiveness of such processes [3]. The nature of the ash deposit depends upon the operating conditions of the gas turbine, particularly the turbine inlet temperature, quality of the fuel, and the characteristics of the intake air. For example, in tests performed using 2–3 ppmw ash particulate in the combustion stream, more deposition and corrosion were observed at a gas temperature of 1260 °C compared with 1093 °C [1]. The observed corrosion characteristics differed from either of those of type I and type II hot corrosion [4,5], or of calcium–magnesium-aluminosilicate (CMAS)-induced failure in thermal barrier coatings (TBCs) [6–10]. The individual effects of CaO and $CaSO_4$ on the degradation of alloys and coatings in the temperature range between 750 and 1150 °C were reported elsewhere [11,12]. In the case of CaO, it directly reacts with Cr_2O_3 and Al_2O_3 scales forming Ca–Cr or Ca–Al ternary compounds, which accelerate degradation including significant spallation under thermal cycling. Although similar adverse effects of such deposits are expected to be observed in syngas-fueled SOFCs as well, especially for metallic interconnects, it has not yet been reported in the literature.

SiO_2 is one of the major ash components from coal- or syngas-fired combustion. The concentration of SiO_2 in the ash varies from nearly zero in the case of some syngas-fired gas turbines [3] up to approximately 50 wt% in the case of pulverized fuel-based power plants [13,14] and oxyfuel systems [14,15]. Even though SiO_2 is not detected from the ash in some applications, it still can be introduced via other sources such as the use of other fuels or ingested air containing SiO_2 during operation. It is also important to understand the effect of the possible ranges of impurities for safe operation. Although being a major ash component, the effects of external SiO_2 on the oxidation characteristics of alloys have not been studied since the non-reactive deposit constituents have been considered as innocuous species in alloy degradation probably because of

* Corresponding author at: National Energy Technology Laboratory, 626 Cochrans Mill Road, Pittsburgh, PA 15236, United States and Department of Mechanical Engineering and Materials Science, University of Pittsburgh, 848 Benedum Hall, Pittsburgh, PA 15261, United States. Tel.: +1 412 624 4208; fax: +1 412 624 8069.
E-mail address: jung.keeyoung@gmail.com (K. Jung).

0378-7753/$ – see front matter © 2011 Elsevier B.V. All rights reserved.
doi:10.1016/j.jpowsour.2010.12.104

their high thermodynamic stability. However, it is necessary to determine whether the deposits are actually benign relative to the degradation of high temperature alloys and coatings and, if not, the mechanism of degradation induced by non-reactive SiO_2 needs to be clearly addressed. Through a combined effort comprises experimental, analytical, and computational modeling approaches, the present study explores detrimental effects of the external SiO_2 particulates on the interfacial failure of Cr_2O_3 oxide layers.

2. Cyclic oxidation experiments

2.1. Experimental details

To study the effect of SiO_2 deposits on the degradation of turbine materials, laboratory cyclic oxidation tests with and without SiO_2 deposits were performed. The alloy used in this study is a directionally solidified (DS) Ni-base superalloy, GTD-111, which is widely used as a first- and second-stage airfoil material in electric power generation gas turbines [16,17]. The nominal composition of the alloy is Ni–14Cr–3Al–9.5Co–2.8Ta–3.8W–1.5Mo–4.9Ti in wt%. In addition, the alloy coated with a platinum-modified nickel aluminide (Pt–NiAl) was studied to compare the differences between outward- and inward-growing oxide layers; GTD-111 alloy is a predominantly outward-growing Cr_2O_3-former, whereas the Pt–NiAl coating is a predominantly inward-growing Al_2O_3-former. The transport mechanism of cations and anions in Cr_2O_3 and Al_2O_3 scales determining the growth directions are well described in the previous literature [18]. Pt–NiAl coatings were prepared by Alcoa Howmet Inc. via a low-activity chemical vapor deposition (CVD) diffusion aluminizing process of Pt-coated GTD-111. Pt–NiAl coatings are mainly used in the hottest sections of gas turbines and as bond coats for thermal barrier coatings (TBCs). The roles and failure mechanisms of these bond coats in TBC systems are well described in the literature [19–21].

The specimens were wet ground through 1200 grit SiC papers to establish controlled surface condition for all test specimens. Subsequently, the specimens were grit-blasted at 207 kPa (=30 psi) for 45 min using 3 μm α-Al_2O_3 powder. Pt–NiAl coated specimens were subjected to the same grit-blasting condition, but without pre-polishing. This provided surface roughnesses (R_a) of uncoated and Pt–NiAl coated specimens which were about 0.3 and 0.5 μm, respectively. After grit-blasting, the specimens were rinsed with water in an ultrasonic bath. The SiO_2 deposits (1.0 ± 0.1 mg cm^{-2}) were then applied to the coupon specimens by spraying an aqueous solution containing the deposit onto all sides of each specimen. The deposited specimens were vertically hung in a sample holder during oxidation. The particle size distribution of SiO_2 powder used in this study was characterized using Photo-Correlation Spectroscopy (PCS, Horiba LB 550) as shown in Fig. 1. The average particle size was 0.98 μm in diameter and the particle size varied between 0.2 and 6.0 μm. The actual ash particle size range in the power plant falls between 0.1 and 60 μm depending on fuel specifications and filtering processes. The particle size and its distribution used in the present experiments, therefore, will represent the smaller side of the practical range. The characterization of the particle size and its distribution is important since it is directly related to the contact area of the underlying materials which may affect the chemical reaction kinetics and it is also related to the possibility of encapsulation in an outward-growing oxide layer.

The cyclic oxidation experiments were performed at 950 °C in furnaces with controlled gas environments. The specimens with dimensions of 15 mm × 10 mm × 3 mm were cycled in and out of the furnace automatically; 45 min in the hot zone, 15 min in the cold zone. The exposures were interrupted to measure mass changes every twenty 1 h-cycles. The deposits remaining unreacted on the specimen were removed in an ultrasonic bath prior to weight change measurements. Then, the SiO_2 was re-deposited for the following 20 h run. After hundred 1 h-cycles, exposures were suspended and the specimens were characterized via optical metallography (OM), X-ray diffractometry (XRD) and scanning electron microscopy (SEM) equipped with an energy-dispersive X-ray spectroscope (EDAX).

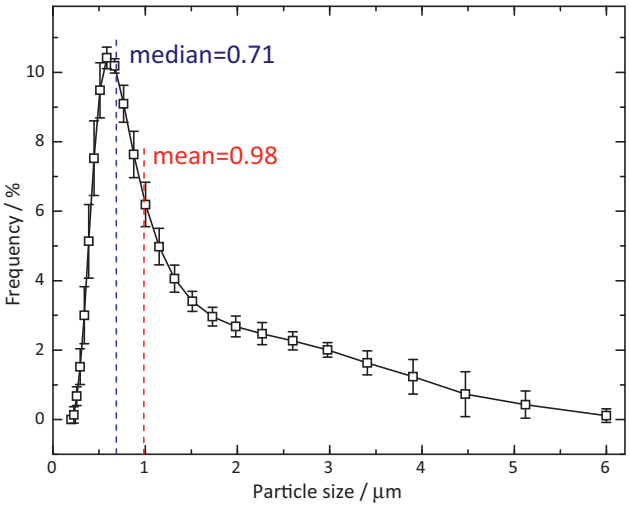

Fig. 1. Particle size distribution of SiO_2 particles used in the present study.

2.2. Specific mass changes and SEM observation

Fig. 2 illustrates the area specific mass changes, Δm_{sp} (mg cm^{-2}), as a function of the number of cycles for uncoated (G0) and Pt–NiAl coated (GP) GTD-111 specimens with SiO_2 deposits exposed at 950 °C for 100 cycles in dry air. The mass changes of the same specimens without SiO_2 deposits are also plotted for comparison. The kinetic curve clearly shows that the deposits have a negligible effect on the mass changes of Pt–NiAl coated GTD-111 (curves (1) GP and (2) GP + SiO_2) whereas there is a considerable effect on those of uncoated alloy (curves (3) G0 and (4) G0 + SiO_2) especially after 40 cycles. The abrupt drop of specific mass change implies the possibility of spallation. The Cr_2O_3 on G0 grows faster than the Al_2O_3

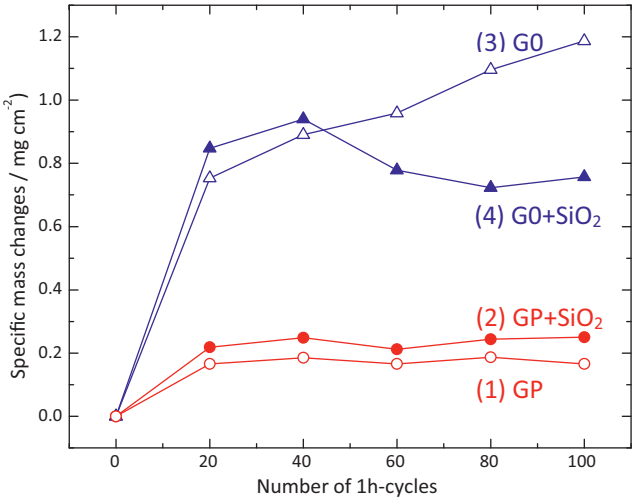

Fig. 2. Specific mass changes versus number of 1 h-cycles. Uncoated GTD-111 (G0) with SiO_2 showed an indication of spallation whereas the effect of SiO_2 on oxidation of Pt–NiAl coated GTD-111 (GP) was negligible.

on GP because the ionic diffusivity of Cr^{3+} through the Cr_2O_3 layer (outward-growing) is much larger than that of O^{2-} across the Al_2O_3 layer (inward-growing).

To further characterize the different kinetic behaviors of the oxide layers, the surfaces and cross-sections of the specimens with and without particles were examined by SEM. Fig. 3 shows surface SEM micrographs for (a) G0 specimen without SiO_2 and (b) G0 with SiO_2 exposed at 950 °C after 100 cycles. Significant spallation of the oxide scale was evident in the presence of SiO_2, as shown in Fig. 3(b) at low magnification (50×). Local areas were enlarged to closely reveal (c) a spalled region, and (d) a TGO retained region at higher magnification (2000×). The micrograph for the spalled region, Fig. 3(c), was characterized via SEM and EDAX as a polycrystalline grain structure of the substrate alloy with fine SiO_2 particles. In Fig. 3(d), it was found that external SiO_2 particles were embedded in the Cr_2O_3 in the regions where the Cr_2O_3 is retained on the surface. This observation is interesting since the encapsulation phenomenon has not been previously reported to our knowledge.

Cross-section micrographs of the G0 with SiO_2 after 100 cycles are presented in Fig. 4 which shows significant amounts of scale buckling, Fig. 4(a), and crack opening at the oxide/alloy interface, Fig. 4(b). Also, it is shown that SiO_2 particles were encapsulated in the Cr_2O_3 as observed from the surface SEM micrographs in Fig. 3. For comparison, the cross-section micrograph for the same specimen (G0) exposed under the same exposure condition, but without SiO_2 deposits, is shown in Fig. 4(c), indicating the adherent oxide/metal interface with a larger TGO thickness.

When the SiO_2 particles are embedded in the Cr_2O_3 TGO, it is expected that the difference in the coefficients of thermal expansion (CTEs) between oxide and alloy ($\Delta\alpha$) will greatly increase since the mean CTE of crystalline SiO_2 ($\alpha = \sim 0.55 \times 10^{-6}\ K^{-1}$ [22]) is more than one order smaller than that of Cr_2O_3 ($\alpha = \sim 7.5 \times 10^{-6}\ K^{-1}$ [22]). Estimation of the critical strain induced by the $\Delta\alpha$ to initiate buckling (ε_b) in G0 with embedded SiO_2 particles will be discussed in more detail in the following section.

On the other hand, the effects of the external SiO_2 deposits on the oxidation characteristics of the GP specimens were quite different from the previously described effects on G0. Fig. 5 shows surface and cross-section micrographs of GP specimens with and without SiO_2 deposits cyclically exposed at 950 °C for 100 cycles. No indication of spallation and encapsulation of the particles was observed, as expected from the kinetic curves in Fig. 2. The typical grain boundary ridges of Pt–NiAl coatings [23] were still evident with a small amount of fine SiO_2 particles sitting on the surface as shown in Fig. 5(c). The observation was also consistent in the cross-sections, Fig. 5(d), showing that the alloy/oxide interface is adherent, and only a small amount of fine SiO_2 particles was observed at the top of the oxide scale. Therefore, the oxide layer remained protective, similar to the case of the layer with no deposits. No major difference was observed between specimens with and without SiO_2 when comparing Fig. 5(a) for GP and Fig. 5(b) for GP with SiO_2. The reason that the particles have not been encapsulated in the TGO can be explained by the very slow- and inward-growing characteristics of the polycrystalline Al_2O_3. Al_2O_3 is known to be a primarily slow inward-growing oxide because of its dense structure with a low defect concentration and the smaller diffusivity of Al^{3+} compared with the diffusivity of O^{2-} across the oxide layer, mainly through its grain boundaries. However, the Al_2O_3 still grows outward to a small extent via the outward cationic transport through the oxide lattice. This growing oxide can 'grab' fine particles and/or lower parts of larger particles during oxidation. For example, small SiO_2 particles sitting on the growing Al_2O_3 oxide surface are clearly seen in Fig. 5(c). The difference in the encapsulation behavior between (a) a fast outward-growing and (b) a slow inward-growing thermal oxide is illustrated in Fig. 6. It shows schematically that external

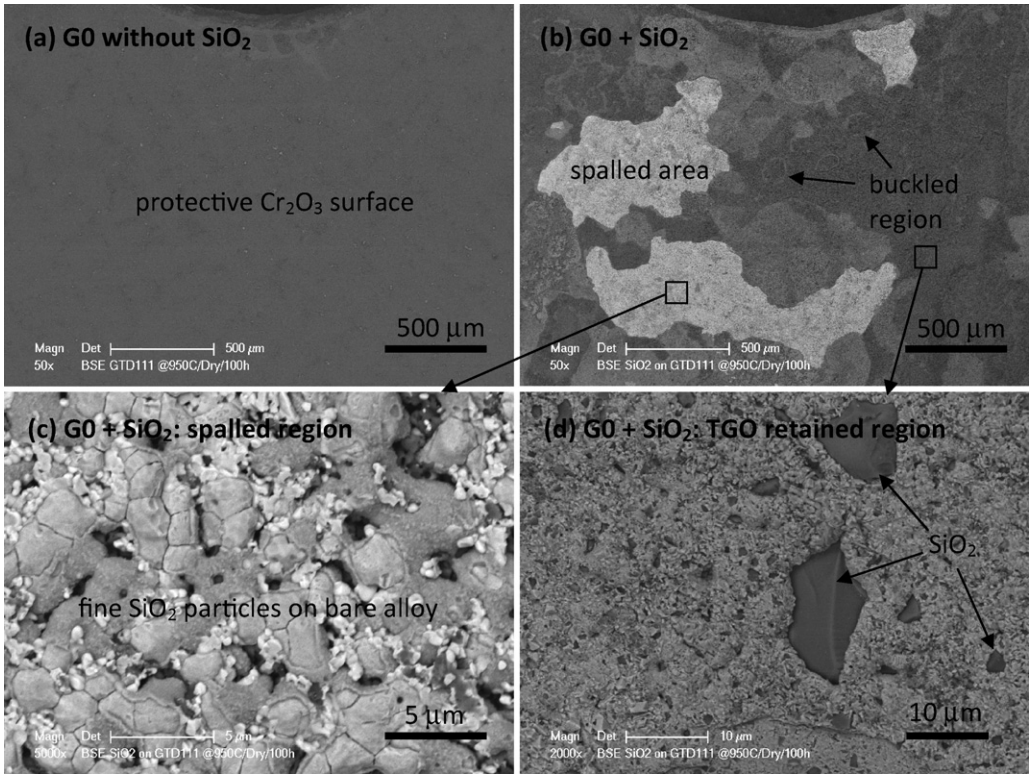

Fig. 3. Surface SEM micrographs of uncoated GTD-111 (G0) with SiO_2 deposits exposed at 950 °C for 100 cycles in air. Spallation is evident in (b) and (c). SiO_2 particles are embedded in a thermally grown Cr_2O_3 layer as shown in (d).

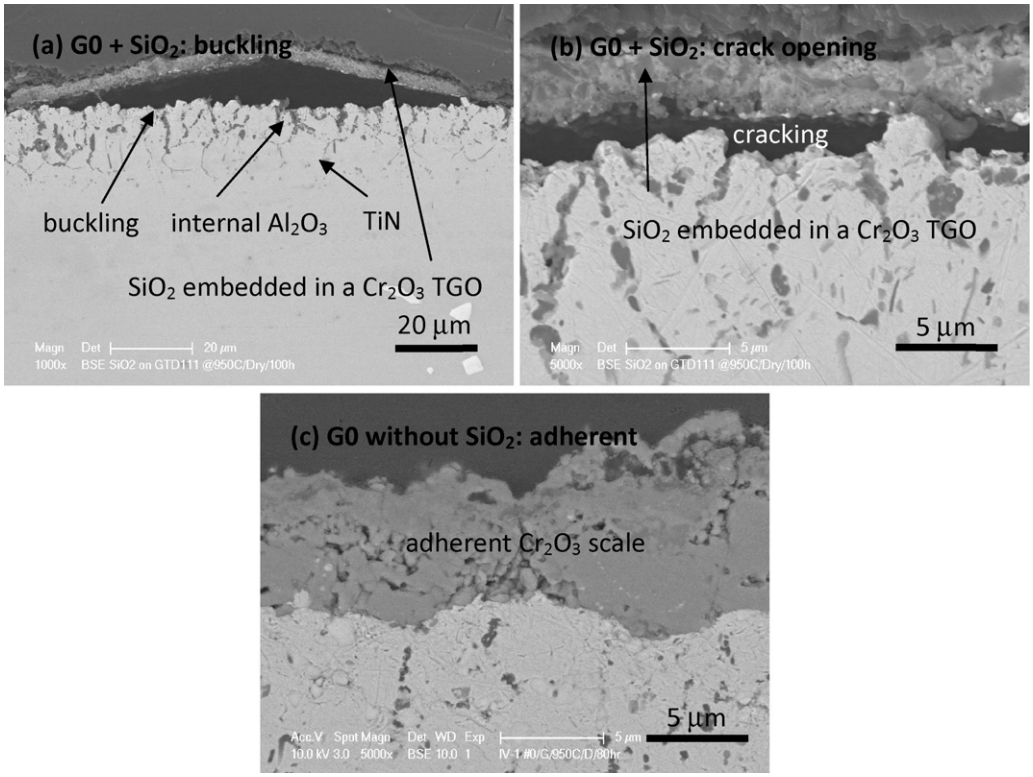

Fig. 4. Cross-section SEM micrographs of uncoated GTD-111 (G0) cyclically exposed at 950 °C in air after 100 cycles with and without SiO_2 deposits. It is shown that (a) buckling and (b) cracking at the metal/oxide interface can occur in the presence of SiO_2, whereas (c) an adherent and protective Cr_2O_3 scale is evident in the absence of SiO_2.

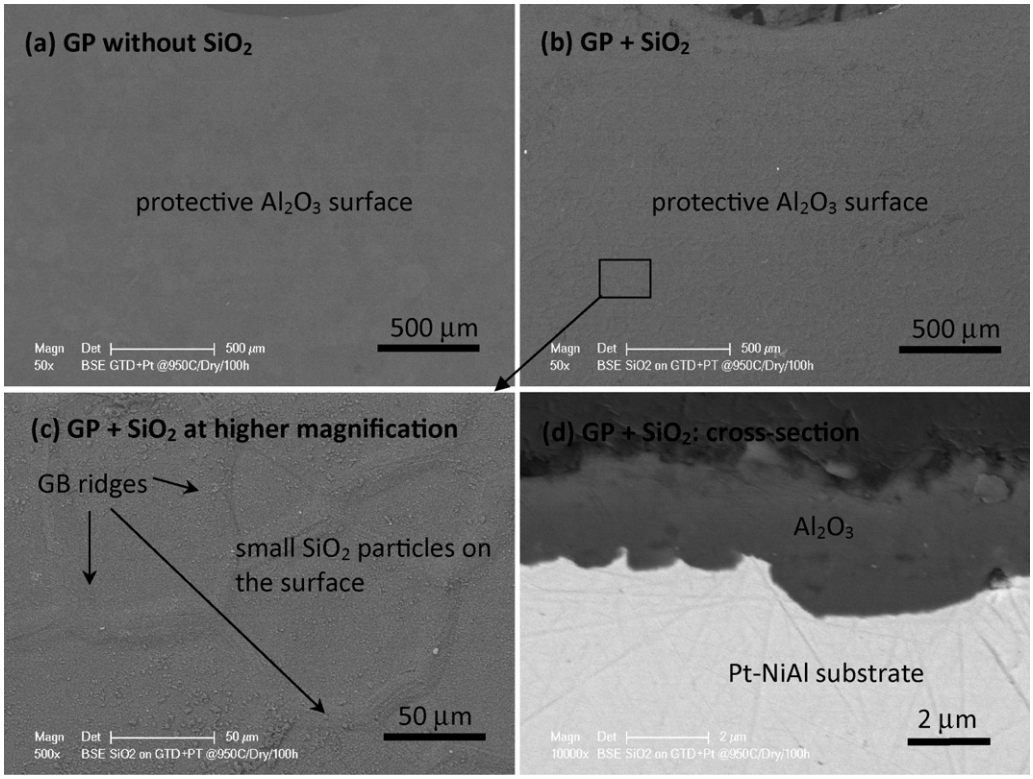

Fig. 5. Surface and cross-section SEM micrographs of Pt–NiAl coated GTD-111 specimens (GP) with and without SiO_2 deposits exposed at 950 °C for 100 cycles in air to show that (b) neither significant spallation nor SiO_2 particle encapsulation in a TGO occurred over the whole surface and (c) grain boundary ridges are still evident indicating that only a thin Al_2O_3 layer is formed on the surface. It is seen that small SiO_2 particles are still sitting on the surface. The surface of GP without SiO_2 is also shown in (a) for comparison. A cross-section micrograph of the specimen is presented in (d) showing that there is no indication of SiO_2 encapsulation.

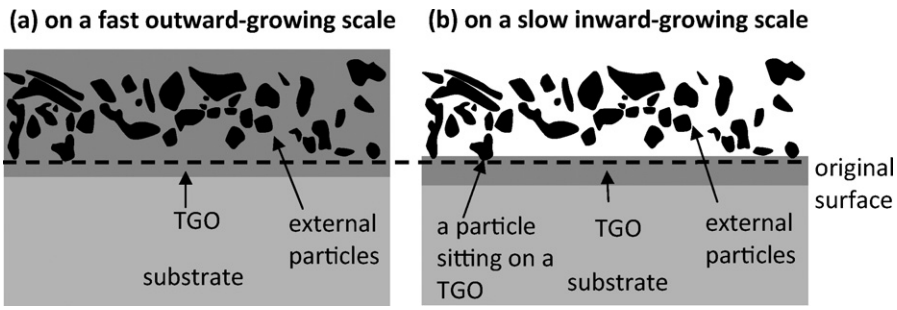

Fig. 6. Cartoons illustrating that (a) external particles can be encapsulated in a fast outward-grown oxide such as Cr_2O_3 scales, and (b) not in a slow inward-growing oxide such as Al_2O_3 scales.

particles can be encapsulated only in a fast outward-growing thermally grown oxide.

3. Numerical analyses

Two methods of analysis were adopted to understand the interfacial failure of a Cr_2O_3 scale in the presence of embedded SiO_2 particles with emphasis on buckling. First, using the classical buckling criterion developed for an ideal flat interface, the thermal strains arising from cooling were estimated and compared with the critical strain for buckling determined based on the experimental observations of the current study. Secondly, Finite Element Analysis (FEA) was utilized to investigate the local distributions of the interfacial shear stresses (τ_{xy}) for idealized microstructures with and without embedded SiO_2 particles. This analysis of the failure via embedded particles was developed based on intensive studies by previous workers [24–31].

3.1. Determination of the critical thermal strain (ε_b) and the critical temperature drop (ΔT_b) for buckling

If it is assumed that (1) an interfacial crack opening occurs in Mode II, i.e., crack surfaces are displaced in sliding mode by shear stress [24], and (2) the substrate alloy, its TGO, and external particulates are under elastic conditions, one may adopt the formulation for the critical buckling stress proposed by Timoshenko and Gere [25] and applied to cases of failure in thermal oxides by Evans et al. [26]. The required stress to cause buckling is represented by:

$$\sigma_b = \left(\frac{1.22E_{ox}}{1-\nu_{ox}{}^2}\right)\cdot\left(\frac{h}{R}\right)^2 \quad (1)$$

in which σ_b is the critical buckling stress; E_{ox} is the elastic modulus of the oxide; ν_{ox} is the Poisson's ratio of the oxide; h is the thickness of the scale; and R is the radius of the interfacial zone of decohesion, respectively. If the only source of stress is derived from differential thermal contraction, the critical thermal strain for buckling is given by:

$$\varepsilon_b = \frac{\sigma_b}{E_{ox}} = \Delta T_b \cdot \Delta\alpha \quad (2)$$

where ε_b is the critical strain to cause buckling and $\Delta\alpha$ is the difference between linear thermal expansion coefficients of metal and oxide ($=\alpha_m - \alpha_{ox}$). Insertion of Eq. (1) into Eq. (2) gives a critical thermal strain to initiate buckling (ε_b), which is:

$$\varepsilon_b = \Delta T_b \cdot \Delta\alpha = \left(\frac{1.22}{1-\nu^2}\right)\cdot\left(\frac{h}{R}\right)^2 \quad (3a)$$

Accordingly, the critical temperature drop, ΔT_b, for buckling with an assumption of a constant $\Delta\alpha$ can be estimated as:

$$\Delta T_b = \left(\frac{1.22}{\Delta\alpha\cdot(1-\nu^2)}\right)\cdot\left(\frac{h}{R}\right)^2 \quad (3b)$$

Most previous work considered the $\Delta\alpha$ as constant with respect to temperature to calculate ε_b and ΔT_b. In the case of Al_2O_3-forming alloys, for example, it is reasonable to assume that the $\Delta\alpha$ is constant since the CTE changes, with increased temperature, of most Al_2O_3-forming alloys are almost parallel to that of the Al_2O_3 oxide layer. In other words, in many cases of Al_2O_3-forming alloys, the slopes of the CTE variations with temperature are similar in alloys and oxides. As a result, the CTE difference between the alloy and its thermally grown Al_2O_3 remains constant at different temperatures. However, in the case of Cr_2O_3-formers, the $\Delta\alpha$ between the alloy and Cr_2O_3 varies largely and non-linearly in different temperature ranges. Therefore, $\Delta\alpha$ should not be assumed to be a constant, and ε_b is more appropriate for a buckling criterion instead of the critical temperature drop. This will be further discussed in a separate publication.

To analytically calculate the thermal strains as a function of temperature drop from 950 °C, the existing CTE data collected from the literature were used. Fig. 7(a) shows instantaneous CTE data for GTD-111 [32], Cr_2O_3 [22], and SiO_2 [22], as well as the calculated upper and lower bounds of CTE of SiO_2 embedded Cr_2O_3. Assuming that the SiO_2/Cr_2O_3 composite is isotropic and the interfaces between SiO_2 and Cr_2O_3 are adherent, one can calculate the lower (isostress condition) and upper bound (isostrain condition) of the CTE for the composite using the following equation based on the balance between the total strain and the sum of strains of each phase:

$$\alpha^n_{composite} = f_{SiO_2}\cdot\alpha^n_{SiO_2} + f_{Cr_2O_3}\cdot\alpha^n_{Cr_2O_3} \quad (4)$$

in which f_{SiO_2} and $f_{Cr_2O_3}$ are the volume fractions of SiO_2 and Cr_2O_3, respectively; n is 1 for the isostrain condition and -1 for the isostress condition. Estimation of volume fraction of a specific component from a cross-sectional area is typically accomplished by using the volume–area proportionality relationship proposed by Delesse [33]. It enables the measurement of the volume fraction of encapsulated SiO_2 in a TGO via a two-dimensional pixel counting method from a digitized map of a representative micrograph (see Fig. 9(a)) providing a value of about 0.29. Based on the collected and calculated data given in Fig. 7(a), the $\Delta\alpha$ between GTD-111 and Cr_2O_3 with and without embedded SiO_2 particles as a function of temperature drop from 950 °C were obtained as shown in Fig. 7(b). The area under each curve in Fig. 7(b) corresponds to a thermal strain, which can be integrated as a middle Riemann sum. Fig. 8 plots these calculated thermal strains as a function of temperature drop from the oxidation temperature of 950 °C with and without the embedded SiO_2 particulates at every 50 K interval.

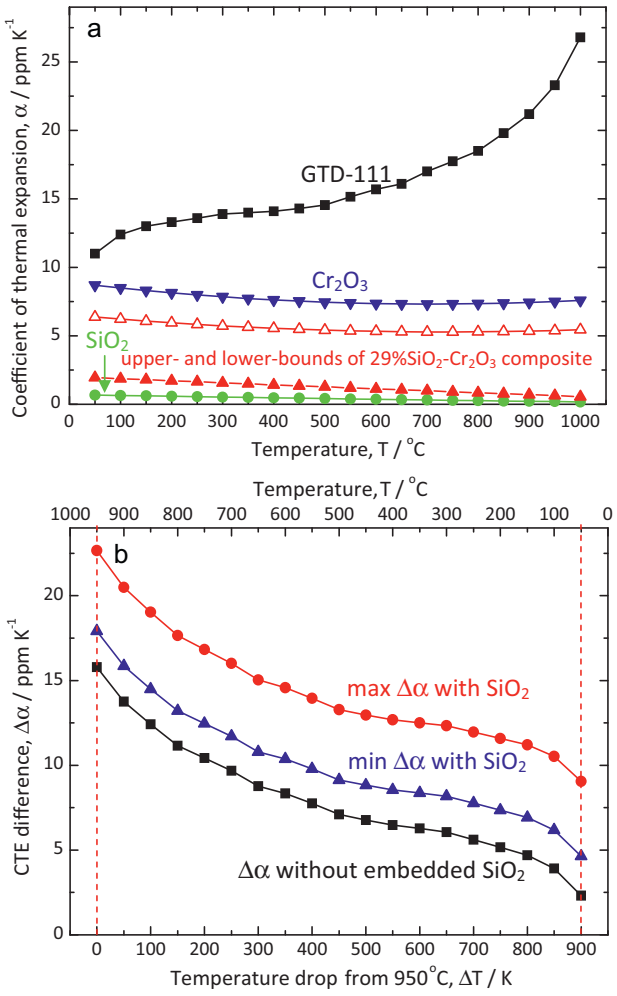

Fig. 7. (a) Instantaneous CTEs of GTD-111, Cr_2O_3, and SiO_2 as well as calculated upper- and lower-bounds of CTEs of a SiO_2-embedded Cr_2O_3 composite and (b) CTE differences with respect to temperature drop from 950 °C between GTD-111 and oxide scales with and without embedded SiO_2. Note that $\Delta\alpha$ with embedded SiO_2 particulates increased because of the low CTE of SiO_2.

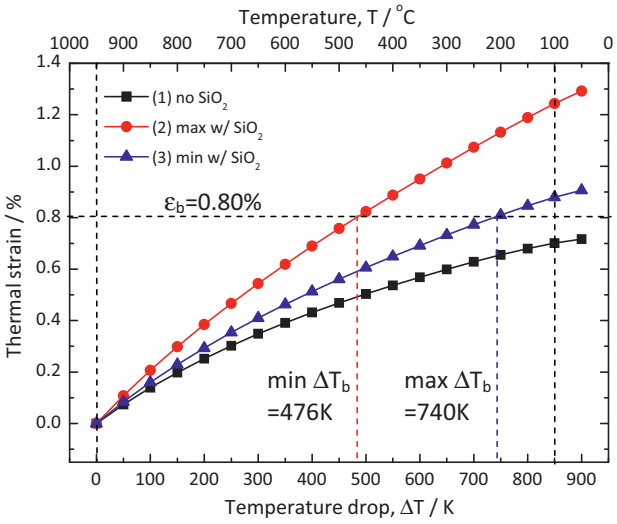

Fig. 8. Calculated thermal strains as a function of temperature drop from 950 °C using data in Fig. 7 along with the critical thermal strain (ε_b = 0.80% elongation) obtained from Eq. (3a) using measured values of parameters from a cross-section micrograph.

Table 1
Elastic properties used in the present study.

Material	Elastic modulus (at 600 °C, MPa)	Poisson's ratio
GTD-111	140.0 [27]	0.29 [27]
Cr_2O_3	260.0 [24]	0.30 [24]
SiO_2	65.7 [24]	0.20 [24]

Additionally, the critical thermal strain to initiate buckling in the present alloy/oxide system can be determined using Eq. (3a) with measured values of the thickness of the scale (h = 4.1 μm on average) and a radius of a buckled zone (R = 53.0 μm) from the observed microstructure such as Fig. 4(a). When the Poisson's ratio of the oxide scale is 0.29, the equation gives a value of ε_b as 0.80%. This means that the oxide scale will buckle when the thermal strain caused by the temperature drop is larger than 0.80%. The ε_b calculated from a buckled microstructure is designated as a horizontal dashed line in Fig. 8. It shows that buckling is expected to occur, with embedded SiO_2, in the temperature drop range 476–740 K (indicated by the two vertical dotted lines) as observed in Fig. 4(a). The temperature drop to initiate buckling is referred as the critical temperature drop for buckling, ΔT_b. However, in the absence of the SiO_2, the calculation predicts that the scale would not buckle up to ΔT = 900 K consistent with the observation in Fig. 4(c), which shows the adherent interface between oxide scale and substrate alloy. Note that the value of ε_b could vary depending on the diameter of the observed buckled region, R, and the local variation of the scale thickness. Sampling of the several cross-sections indicated that the diameter of the buckled zone varies between 44.7 and 76.1 μm; thus, it is not unreasonable to assume the measured value from the cross-section (R = 53.0 μm and h = 4.1 μm on average over a long range) can be taken as a representative of the buckled zone. The elastic properties used in the calculation are summarized in Table 1. Although the elastic properties of directionally solidified GTD-111 will vary along different loading directions [34], the averaged value over all loading directions was assumed as a representative of the alloy.

Based on the calculational analyses, it can be additionally predicted that the dramatic effect of the encapsulated particles can be reduced in the case of the external particles with higher CTEs than those of SiO_2 ($\alpha = \sim 0.55 \times 10^{-6}\,K^{-1}$), such as Fe_2O_3 deposits ($\alpha = \sim 13.8 \times 10^{-6}\,K^{-1}$ [22]), which are closer to those of the substrate alloy since it will decrease the CTE difference between metal and oxide leading to smaller thermal strains.

Although this classical buckling criterion can be used to evaluate this type of interfacial failure caused by the encapsulated particles in a thermal oxide, several issues must be resolved. For example, important aspects that need to be considered are the amount of particulates encapsulated in a thermal oxide and the cause of this encapsulation. It seems that the volume fraction of embedded particulates varies as a function of growth rate of a thermal oxide. If this is the case, oxidation temperature, time, and kinetic constants associated with defect structure of the oxide will be related to the volume fraction of embedded particles. The ratio of particulate size to oxide thickness (r/h) will be important as well. Studies to determine the factors that control the volume fraction of embedded particles in a thermal oxide during growth may be interesting.

3.2. Calculation of the local shear stresses at metal/oxide interface via FEA

To further understand the localized effect of embedded SiO_2 particles in a Cr_2O_3 scale on interfacial failure of the oxide scale, the changes in stress distributions during cooling were calculated using two-dimensional finite element analysis (FEA). The calcu-

lated results via the FEA will be discussed in terms of the shear stresses (τ_{xy}) at the metal/oxide interface that should play an important role on decohesion of the oxide scale from the substrate required for buckling failure. The discussion starts with a description of a method to create idealized microstructures from experimental observation to use as an initial microstructure for the simulation. Subsequently, details for the cooling simulation are described. The interfacial shear stresses calculated from the simulation will be discussed to elucidate the role of embedded particles on decohesion of the oxide scale.

3.2.1. Generation of an idealized microstructure from a real microstructure

To perform a more realistic calculation, one of the cross-sectional microstructures representing interfacial delamination in Fig. 4(b) was selected and digitized for the calculation. All the major interfaces among embedded SiO_2 particulates, a Cr_2O_3 scale, and a GTD-111 substrate were traced to create a simplified microstructure as in Fig. 9(a). For the generation of the simplified microstructure, it was assumed that: (1) there is no pre-existing crack at the oxide/metal interface and, therefore, the interface is adherent in the digitized microstructure and (2) only major constituents (substrate alloy, Cr_2O_3 TGO, and large embedded SiO_2 particulates) were included in the simplified microstructure, i.e., all other minor constituents in the oxide and substrate were neglected. The traced microstructure was implanted into an FEM mesh via the OOF package (the Object-Oriented Finite element code developed by the National Institute of Standards and Technology, Gaithersburg, MD [35]) using an adaptive mesh generation algorithm. The resulting mesh structures created by the described protocol are shown in Fig. 9(a) and (b) representing the idealized microstructures with and without embedded SiO_2, respectively. The microstructure without embedded particles in Fig. 9(b) was generated by eliminating the embedded particles from the microstructure in Fig. 9(a).

3.2.2. Local shear stress distribution along metal/oxide interface

As previously noted, the residual shear stress distribution (τ_{xy}) arising from temperature changes is an important measure to describe 'decohesion' of an oxide layer from the substrate alloy. The τ_{xy} distributions were calculated through a cooling simulation via a commercial FEA package, ABAQUS (Abaqus Inc., Providence, RI) [36]. During the calculation, it was assumed that (1) all the phases are homogeneous, isotropic, and ideally elastic; and (2) stress-relieving mechanisms, such as creep, phase transformation, crack formation, are not operating during the simulation. It was also assumed that (3) the thermo-mechanical parameters for the constituent phases do not vary with respect to temperature except for the CTEs which instantaneously vary with temperature. The parameters used in the simulation were the same as previously used in Section 3.1. A mixture of fixed and free boundary conditions (BC) was used for the displacement of each element along x (horizontal) and y (vertical) directions; the free BCs were assigned to the all boundary elements but the displacements of elements along $\pm x$ on the left and $\pm y$ on the bottom sides were set to be fixed. To exclude the computational artifact for the free boundary condition arising from a relatively small computational section, the meshed microstructure in Fig. 9(a) was extended (ten times along the $+x$ direction using mirror images, and the four times along the $-y$ direction by enlarging the substrate region) as given in Fig. 9(c).

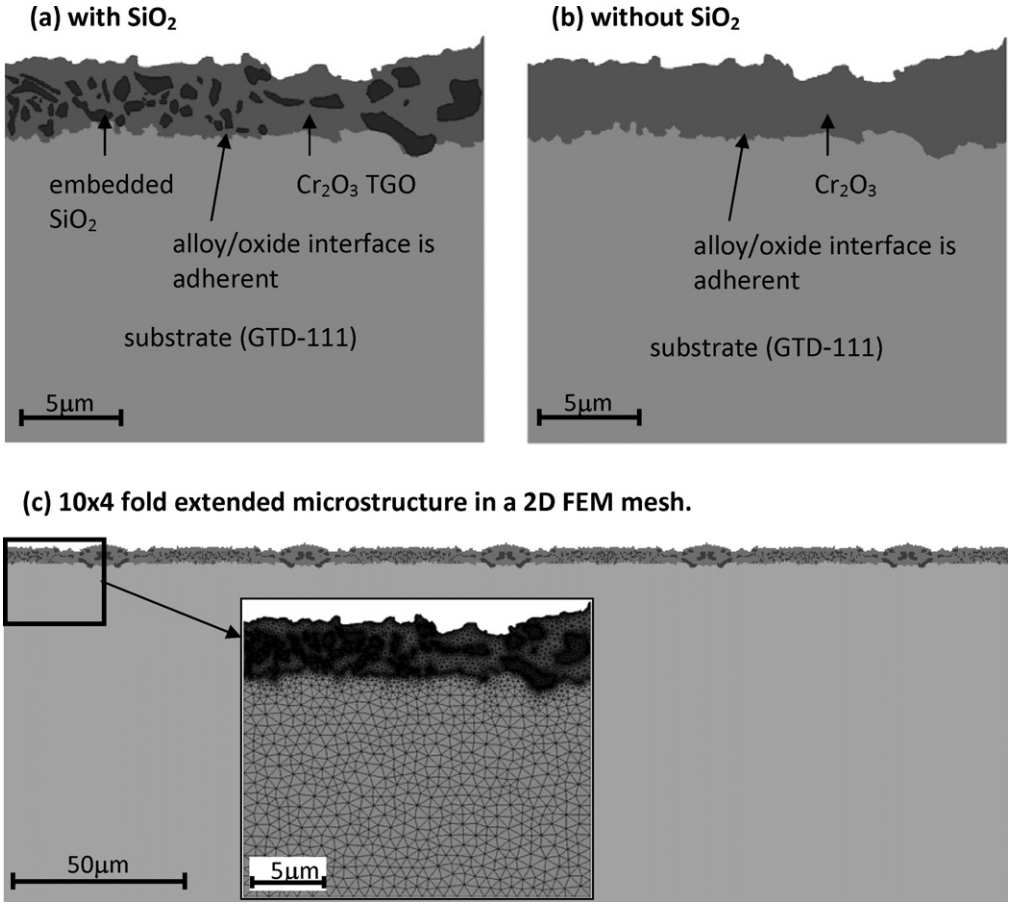

Fig. 9. (a) An idealized microstructure using a real microstructure in Fig. 4(b), (b) a hypothetical idealized microstructure but with no embedded SiO_2, and (c) a 10×4 fold extended microstructure implanted in a 2D FEM mesh.

The first section (out of ten repetitive sections) of the extended domain at the top-left corner was then selected as representative of the simulation results as indicated with a rectangle in Fig. 9(c). Preliminary calculations (not shown in the paper) confirmed that this pseudo-periodic boundary condition effectively eliminates the spurious computations. The plane strain condition was used assuming that the normal strain ε_{zz} and the shear strains γ_{xz} and γ_{yz} are negligibly small compared with the cross-sectional strains. For comparison, the same extension and subsequent calculation was repeated but with a hypothetical microstructure without embedded SiO_2 in Fig. 9(b). The cooling simulation extends from 950 °C down to 20 °C and the stress distributions were monitored at every 50 K of the temperature drop.

Fig. 10 shows the absolute values of τ_{xy}, $|\tau_{xy}|$, along the metal/oxide interface for the microstructures with (in red) and without (in blue) SiO_2 particles induced by a temperature drop of $\Delta T = -930$ K, i.e., at $T = 20$ °C. Since the sign of τ_{xy} simply represents the direction of the shear stress, their absolute values were plotted. The plot shows that $|\tau_{xy}|$ scatters in the ranges of ±2.5 and ±1.2 GPa for the microstructures with and without SiO_2 particles, respectively. The average values of $|\tau_{xy}|$ are 475.3 (with SiO_2) and 322.2 (without SiO_2) MPa. The result implies that the presence of embedded SiO_2 particles in a Cr_2O_3 scale will increase $|\tau_{xy}|$ and, consequently lead to a higher probability of the oxide decohesion from substrate. Such detrimental impact by the encapsulated particles can also be clarified by the position of $|\tau_{xy}|$. The equilibrated microstructure after cooling is also shown on top of the plot to qualitatively show the dependency of the location of the embedded particles on the interfacial shear stresses. It can be seen that $|\tau_{xy}|$ at the interface tends to be greatly amplified by about 50% on average and locally up to about 300% when the SiO_2 particulates are located near the interface. Also, the resulting shear stresses seem to become even larger near larger particles as indicated with arrows in the figure. It infers that, in the presence of embedded SiO_2 particles, decohesion of the oxide scale can occur even when the average shear stress over the entire interface is smaller than the critical shear stress for decohesion because the amplified local shear stresses near the particles can be greater than the critical shear stress. This amplification of the shear stress will be important to determine whether the interfacial failure occurs in mode I or II when the normal thermal strain (ε_{xx}) during cooling is large enough for both mechanisms. If the amplification by the presence of SiO_2 is critical to cause decohesion, the failure mode II, i.e., buckling of the oxide scale after the preceding decohesion at the metal/oxide interface, will operate preferentially. Otherwise, the failure mode I, i.e., wedging crack through the oxide scale and the subsequent decohesion, will be predominant.

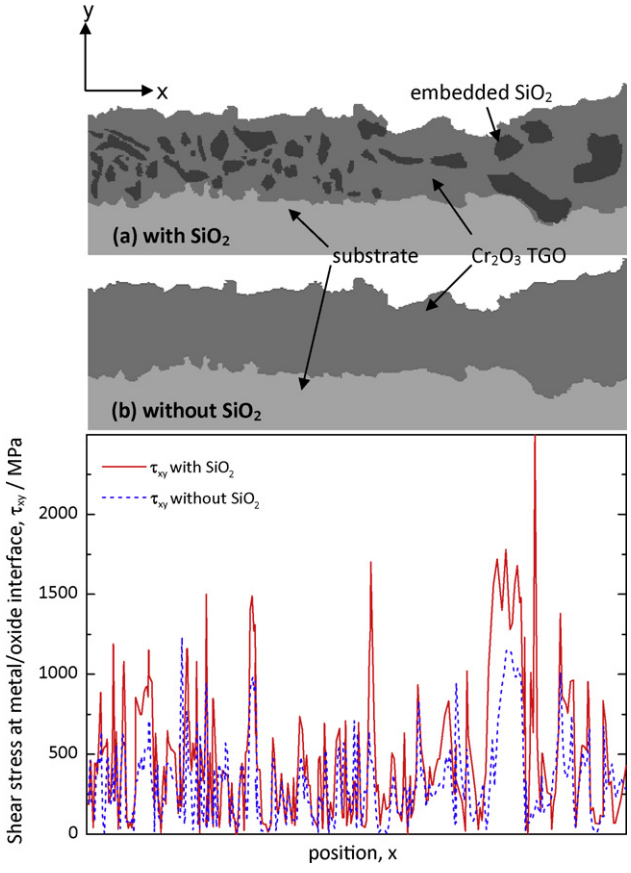

Fig. 10. Calculated local thermal shear stresses (τ_{xy}) along the metal/oxide interfaces after cooling ($\Delta T = -930$ K from 950 °C) obtained from the equilibrated microstructures (a) with and (b) without embedded SiO_2 particles. It is shown that the local shear stresses are significantly amplified in the presence of the embedded SiO_2, especially when the particles are located in the vicinity of the interface.

Although the critical interfacial shear strength between Cr_2O_3 and the GTD 111 alloy is not currently available, it is expected that the amplification of the shear stress can be critical to initiate crack formation at the interface. For example, for Cr_2O_3-forming Crofer 22 APU which is an Fe–22Cr–0.5Mn alloy widely used as a metallic interconnect for SOFC applications, the critical interfacial shear strength was estimated as 442.5 (STD = 15.2) MPa by Sun et al. when the Cr_2O_3 thickness is in the range 2.06–2.98 μm [37]. Assuming that the critical shear strength of Cr_2O_3/Crofer is not much different from that of Cr_2O_3/GTD-111 with the TGO thickness of 4.1 μm, the calculated local shear stresses can be roughly evaluated to see whether the amplified local shear stress would be sufficient to initiate decohesion. Recalling that the average values of $|\tau_{xy}|$ are 475.3 (with SiO_2) and 322.2 (without SiO_2) MPa from the FEA, it is inferred that the presence of SiO_2 can be critical to cause interfacial decohesion. For a more accurate evaluation, the shear stress distribution tangential to the local interface and the shear strength for this particular interface will be required. It should be noted that the maximum shear stress (τ_{max}) at the edge on the right side of the interface decreases as the lateral dimension of the finite specimen increases as predicted by Tien and Davidson; $\tau_{max} \propto 1/L$, where L is the width of the specimen [31]. Also, the shear stress along the interface decreases from the edge to the center of the specimen. The $|\tau_{xy}|$ distributions near the center region, i.e., at the squared region in Fig. 9(c), represent minimal effects of particle encapsulation in the entire specimen. These SiO_2 particle effects will be even more amplified near the edge region of the specimen especially when the specimen size is small.

4. Conclusion

The present paper describes a new interfacial failure mode induced by the presence of chemically inert external SiO_2 particles that can be accumulated on interior hardware for syngas-fired power generation. Accelerated cyclic oxidation tests were performed to provide examples of the failure. The experimental results showed that the SiO_2 caused (1) spallation and buckling on a Cr_2O_3-former (GTD-111) although the amount of the attack is much less significant than that induced by CaO, and (2) a negligible effect on an Al_2O_3-former (Pt–NiAl). The difference was explained by the rapidly outward-growing and the slowly inward-growing characteristics of Cr_2O_3 and Al_2O_3 layers, respectively. The buckling failure of the SiO_2 embedded Cr_2O_3 TGO on GTD-111 was analytically accessed by a modified version of a classical buckling criterion. The analyses showed that the CTE differences ($\Delta\alpha$) and the resulting thermal strains (ε_{th}) between oxide and substrate alloy can

be greatly increased via encapsulation of external SiO_2. The calculated thermal strains were compared with the critical strain for buckling (ε_b) obtained from the observed microstructure leading to a prediction of the critical temperature drop for buckling (ΔT_b) as 476–740 K in the presence of embedded SiO_2. This detrimental effect of SiO_2 particles was further investigated by FEA simulation. It is concluded from the simulation that the localized shear stresses (τ_{xy}) at the metal/oxide interface will be significantly increased especially in the vicinity of encapsulated particles that can lead to accelerated decohesion which is a pre-requisite condition for buckling.

In summary, based on the experimental observations and calculational analyses, the interfacial failure in the presence of SiO_2 predominantly occurs as follows:

(1) The external SiO_2 particles are encapsulated in the outward-growing Cr_2O_3 scale during oxidation.
(2) The overall CTEs of the oxide composite are decreased due to the embedded particles with low CTEs such that the CTE differences between metal and oxide, and therefore the resulting thermal strains are increased.
(3) The increased thermal strains lead to amplification of the shear stresses (τ_{xy}) at the metal/oxide interface that may result in accelerated decohesion.
(4) When the increased thermal strains exceed the critical strain for buckling (ε_b), scale buckling occurs.

Although the alloy systems and temperature used in the present study were taken from syngas-fueled gas turbines to demonstrate the effect of chemically inert external oxide particles, the same mechanism can be applied to other particle-associated high temperature applications, such as syngas-fueled SOFCs or coal-fired oxyfuel systems.

Acknowledgements

This work at the University of Pittsburgh was performed in support of the U.S. DOE and the National Energy Technology Laboratory (NETL) under the UTSR subcontract 04-01-SR-116 and the RES contract DE-FE0004000, respectively. The work performed at the University of Wisconsin at Milwaukee was supported by the start-up fund from the college of engineering and applied science for C.-S. Kim. The authors gratefully acknowledge GE Energy for providing specimens.

References

[1] R.A. Wenglarz, Impact of Alternative Fuels on Turbine Materials, Materials Workshop III, DOE, University of Connecticut, CT, 2002.
[2] W.T. Reed, External Corrosion and Deposits, American Elsevier Publishing Co. Inc., New York, 1971.
[3] I.G. Wright, T.B. Gibbons, Int. J. Hydrogen Energy 32 (2007) 3610–3621.
[4] R.A. Wenglarz, I.G. Wright, in: R. Viswanathan, J. Stringer (Eds.), Materials and Practices to Improve Resistance to Fuel Derived Environmental Damage in Land- and Sea-Based Turbines, EPRI 1009173, Palo Alto, 2003, pp. 4-45–4-66.
[5] N. Birks, G.H. Meier, F.S. Pettit, Introduction to High Temperature Oxidation of Metals, second ed., Cambridge University Press, Cambridge, 2006.
[6] M.P. Borom, C.A. Johnson, L.A. Peluso, Surf. Coat. Technol. 86–87 (1996) 116–126.
[7] C. Mercer, S. Faulhaber, A.G. Evans, R. Darolia, Acta Mater. 53 (2005) 1029–1039.
[8] S. Krämer, S. Faulhaber, M. Chambers, D.R. Clarke, C.G. Levi, J.W. Hutchinson, A.G. Evans, Mater. Sci. Eng. A 490 (2008) 26–35.
[9] A.G. Evans, D.R.D.R. Clarke, C.G. Levi, J. Eur. Ceram. Soc. 28 (2008) 1405–1419.
[10] R.G. Wellman, J.R. Nicholls, Tribol. Int. 41 (2008) 657–662.
[11] K.T. Chiang, G.H. Meier, R.A. Perkins, J. Mater. Eng. 6 (1984) 71–86.
[12] K. Jung, F.S. Pettit, G.H. Meier, Mater. Sci. Forum 595–598 (2008) 805–812.
[13] B.G. Kutchko, A.G. Kim, Fuel 85 (2006) 2537–2544.
[14] B. Bordenet, F. Kluger, Mater. Sci. Forum 595–598 (2008) 261–269.
[15] G.R. Holcomb, Annual NETL CO_2 Capture Technology for Existing Plants R&D Meeting, Pittsburgh, PA, 2009.
[16] P.W. Schilke, GE Energy Report, GER 3569G, General Electric Company, New York, 2004.
[17] A.P. Gordon, M.D. Trexler, R.W. Neu, T.J. Sanders Jr., D.L. McDowell, Acta Mater. 55 (2007) 3375–3385.
[18] W.J. Quadakkers, I.I. Holzbrecher, K.G. Briefs, H. Beske, Oxid. Met. 32 (1989) 67–88.
[19] A.G. Evans, D.R. Mumm, J.W. Hutchinson, G.H. Meier, F.S. Pettit, Prog. Mater. Sci. 46 (2001) 505–553.
[20] R.A. Ruud, A. Bartz, M.P. Borom, C.A. Johnson, J. Am. Ceram. Soc. 84 (7) (2001) 1545–1552.
[21] N.M. Yanar, F.S. Pettit, G.H. Meier, Metall. Mater. Trans. A 37 (4) (2006) 1563–1580.
[22] Y.S. Touloukian, R.K. Kirby, E.R.E.R. Taylor, T.Y.R. Lee, Thermophysical Properties of Matter – the TPRC Data Series. Volume 13: Thermal Expansion – Nonmetallic Solids, IFI/Plenum, New York, 2002.
[23] Y. Zhang, W.Y. Lee, J.A. Haynes, I.G. Wright, B.A. Pint, K.M. Cooley, P.K. Liaw, Metall. Mater. Trans. A 30 (1999) 2679–2687.
[24] H.E. Evans, R.C. Lobb, Corros. Sci. 24 (3) (1984) 209–222.
[25] S.P. Timoshenko, J.M. Gere, Theory of Elastic Stability, McGraw-Hill, New York, 1961.
[26] H.E. Evans, G.P. Mitchell, R.C.R.C. Lobb, D.R.J. Owen, Proc. R. Soc. A 440 (1993) 1–22.
[27] W. Christl, A. Rahmel, M. Schütze, Oxid. Met. 31 (1989) 1–34.
[28] M. Schütze, Oxid. Met. 44 (1995) 29–61.
[29] M. Schütze, Protective Oxide Scales and their Breakdown, Wiley, Chichester, 1997.
[30] M. Schütze, P.F. Tortorelli, I.G. Wright, Oxid. Met. 73 (2010) 389–418.
[31] T.K.J.K. Tien, J.M. Davidson, in: J.V. Cathcart (Ed.), Stress Effects and the Oxidation of Metals Proc., TMS-AIME Fall Meeting 1974, AIME, New York, 1975, pp. 200–219.
[32] M.D. Trexler, B.C. Church, T.H. Sanders Jr., Scr. Mater. 55 (2006) 561–564.
[33] M. Delesse, Ann. Mine. 13 (1862) 379–388.
[34] M.M. Shenoy, D.L. McDowell, R.W. Neu, Int. J. Plasticity 22 (2006) 2301–2326.
[35] http://www.nist.gov/msel/ctcms/oof/.
[36] http://www.simulia.com/.
[37] X. Sun, W.N. Liu, E. Stephens, M.A. Khaleel, J. Power Sources 176 (2008) 167–174.